

UCLA

UCLA Previously Published Works

Title

Simultaneous pH-sensitive and oxygen-sensitive MRI of human gliomas at 3 T using multi-echo amine proton chemical exchange saturation transfer spin-and-gradient echo echo-planar imaging (CEST-SAGE-EPI)

Permalink

<https://escholarship.org/uc/item/5wn372jw>

Journal

Magnetic Resonance in Medicine, 80(5)

ISSN

0740-3194

Authors

Harris, Robert J

Yao, Jingwen

Chakhoyan, Ararat

et al.

Publication Date


2018-11-01

DOI

10.1002/mrm.27204

Peer reviewed

Simultaneous pH-sensitive and oxygen-sensitive MRI of human gliomas at 3 T using multi-echo amine proton chemical exchange saturation transfer spin-and-gradient echo echo-planar imaging (CEST-SAGE-EPI)

Robert J. Harris^{1,2,3*} | Jingwen Yao^{1,2,5*} | Ararat Chakhoyan^{1,2} |
 Catalina Raymond^{1,2} | Kevin Leu^{1,2,3} | Linda M. Liao^{7,8} | Phioanh L. Nghiemphu⁴ |
 Albert Lai^{4,7} | Noriko Salamon² | Whitney B. Pope² | Timothy F. Cloughesy⁴ |
 Benjamin M. Ellingson^{1,2,3,5,6,7} 

¹UCLA Brain Tumor Imaging Laboratory, Center for Computer Vision and Imaging Biomarkers, David Geffen School of Medicine, University of California Los Angeles, Los Angeles, California

²Department of Radiological Sciences, David Geffen School of Medicine, University of California Los Angeles, Los Angeles, California

³Physics and Biology in Medicine, David Geffen School of Medicine, University of California Los Angeles, Los Angeles, California

⁴Department of Neurology, David Geffen School of Medicine, University of California Los Angeles, Los Angeles, California

⁵Department of Bioengineering, Henry Samueli School of Engineering and Applied Science, University of California Los Angeles, Los Angeles, California

⁶Department of Psychiatry and Biobehavioral Sciences, David Geffen School of Medicine, University of California Los Angeles, Los Angeles, California

⁷UCLA Brain Research Institute, David Geffen School of Medicine, University of California Los Angeles, Los Angeles, California

⁸Department of Neurosurgery, David Geffen School of Medicine, University of California Los Angeles, Los Angeles, California

Correspondence

Benjamin M. Ellingson, Associate Professor of Radiology, Biomedical Physics, Psychiatry, and Bioengineering; Director of UCLA Brain Tumor Imaging Laboratory; Departments of Radiological Sciences and Psychiatry, David Geffen School of Medicine, University of California, Los Angeles, 924 Westwood Blvd., Suite 615, Los Angeles, CA 90024.

Email: bellingson@mednet.ucla.edu;

Twitter: @ben_ellingson

Funding information

American Cancer Society Research Scholar Grant (RSG-15-003-01-CCE) (B.M.E.); Art of the Brain (T.F.C.); University of California Research Coordinating Committee (B.M.E.); UCLA Jonsson Comprehensive Cancer Center Seed Grant (B.M.E.); UCLA SPORE in Brain Cancer (NIH/NCI

Purpose: To introduce a new pH-sensitive and oxygen-sensitive MRI technique using amine proton CEST echo spin-and-gradient echo (SAGE) EPI (CEST-SAGE-EPI).

Methods: pH-weighting was obtained using CEST estimations of magnetization transfer ratio asymmetry (MTR_{asym}) at 3 ppm, and oxygen-weighting was obtained using R'_2 measurements. Glutamine concentration, pH, and relaxation rates were varied in phantoms to validate simulations and estimate relaxation rates. The values of MTR_{asym} and R'_2 in normal-appearing white matter, T_2 hyperintensity, contrast enhancement, and macroscopic necrosis were measured in 47 gliomas.

Results: Simulation and phantom results confirmed an increase in MTR_{asym} with decreasing pH. The CEST-SAGE-EPI estimates of R_2 , R_2^* , and R'_2 varied linearly with gadolinium diethylenetriamine penta-acetic acid concentration ($R_2 = 6.2 \text{ mM}^{-1} \cdot \text{sec}^{-1}$ and $R_2^* = 6.9 \text{ mM}^{-1} \cdot \text{sec}^{-1}$). The CEST-SAGE-EPI and Carr-Purcell-Meiboom-Gill estimates of R_2 ($R^2 = 0.9943$) and multi-echo gradient-echo estimates of R_2^* ($R^2 = 0.9727$) were highly correlated. T_2 lesions had lower R'_2 and higher MTR_{asym} compared with normal-appearing white matter, suggesting lower hypoxia and high acidity, whereas contrast-enhancement tumor regions had elevated R'_2 and MTR_{asym} , indicating high hypoxia and acidity.

Robert J. Harris and Jingwen Yao contributed equally to this work.

IP50CA211015-01A1) (B.M.E., L.M.L., P.L.N., A.L., W.B.P., T.F.C.); NIH/NCI IR21CA223757-01 (B.M.E.)

Conclusion: The CEST-SAGE-EPI technique provides simultaneous pH-sensitive and oxygen-sensitive image contrasts for evaluation of the brain tumor microenvironment. Advantages include fast whole-brain acquisition, in-line B_0 correction, and simultaneous estimation of CEST effects, R_2 , R_2^* , and R_2' at 3 T.

KEY WORDS

CEST, glioma, hypoxia, pH-weighted MRI, SAGE

1 | INTRODUCTION

Abnormal metabolism is a hallmark of cancer.^{1,2} Notably, glycolysis is often enhanced in cancers, even in the presence of abundant oxygen (i.e., the Warburg effect²) (Figure 1). This form of aerobic glycolysis results in a dramatic decrease in extracellular pH due to increased concentration of lactic acid.¹ This increase in extracellular acidity comes with dramatic consequences, as it can be directly linked to the degree of tumor aggressiveness^{3,4} and increases tumor invasion.^{5,6} Interestingly, histological evidence suggests regions containing pseudopalisades, a pathological trademark of glioblastoma, are also hypoxic, express extracellular matrix proteases, and are the result of active tumor migration.⁷ Increased acidity within the tumor also has been shown to lead to decreased immune function.⁸ The acidic micro-environment in tumors is also conducive to elevated vascular endothelial growth factor expression⁹ and expression of platelet-derived endothelial cell growth factor,¹⁰ which has been shown to result in increased angiogenesis. This in turn leads to a positive feedback process, leading to further tumor growth, decreasing oxygen tension, increased hypoxia, and increasing glycolysis, resulting in increased lactic acid, decreasing extracellular tissue pH, and more mutations and/or adaptations of the tumor genome. Thus, extensive *in vitro*, preclinical, and clinical evidence appears to support the hypothesis that tumor acidity and oxygen metabolism both play a critical role in gliomagenesis. There remains, however, a critical need in furthering our understanding of the role of extracellular acidosis and oxygen metabolism in human gliomas and its clinical relevance due to the lack of a robust noninvasive tool for simultaneously estimating and localizing regions of low pH and oxygen consumption. Thus, the purpose of the study was to develop a new, noninvasive MRI technique that can provide high-resolution images with sensitivity to tumor acidity and oxygen metabolism that can be performed on clinical MRI systems.

1.1 | pH-weighted metabolic MRI using CEST contrast from fast exchangeable amine protons on glutamine

In addition to glucose, glutamine is also a major source of fuel for malignant tumors.¹¹ It is essential for cellular

proliferation, tumor growth, and tumor cell survival. Glutamine is the most abundant amino acid in the body, circulating at concentrations of 0.6 to 0.9 mM and as high as 20 mM in tissue.¹¹ Tumor cells often consume a significant amount of glutamine,¹² acting at times like a “glutamine trap.” Glutamine demand is so high that transport systems are amplified to increase glutamine consumption.¹³ Glutamine has 2 nitrogen functional groups, an amine and an amide group, having hydrogen NMR resonance frequencies of 3.0 and 3.5 ppm, respectively, compared with water protons. The chemical exchange between amine and amide protons in bulk water has been shown to be pH dependent using a new imaging method called CEST imaging.¹⁴ The inherently elevated concentration of glutamine within tumors further increases the available proton exchange, resulting in a higher CEST signal at 3.0 ppm.^{15,16} The combination of increased protons (low pH) and increased glutamine makes pH-weighted MRI using CEST contrast from amine protons on glutamine particularly attractive as a noninvasive tool for assessment of microenvironment acidity within malignant brain tumors.

1.2 | R_2' -based BOLD imaging

The level of glycolysis depends on both the accumulation of lactic acid and the inefficient use of oxygen. Thus, image maps that are sensitive to tumor oxygen metabolism are critically important for understanding the relative level of aerobic (pathologic) versus anaerobic (normal) glycolysis. Blood oxygen level-dependent imaging, based on the contrast mechanisms routinely used for functional imaging (fMRI), allows for noninvasive estimation of blood or tissue oxygenation. Simply stated, oxygenated blood containing oxyhemoglobin is diamagnetic, as the iron at the core is magnetically shielded from blood water, resulting in coherent MR spins and a high MR signal. Early studies from Ogawa et al¹⁷ confirmed this in mice breathing high concentrations of oxygen. In deoxygenated blood, the iron is exposed to blood water, resulting in magnetic interference with the proton magnetic moment on water molecules. This interference results in incoherent MR spins and signal dropout in the areas of high deoxyhemoglobin concentration. The paramagnetic nature of deoxyhemoglobin enhances the effective transverse relaxation rate R_2^* . Changes in tissue R_2^* therefore reflect relative

changes in concentration of deoxyhemoglobin, and thus an indirect measure of oxygen extraction fraction (OEF). Use of the reversible transverse relaxation rate, $R_2' = R_2^* - R_2$, both isolates the local susceptibility effect while compensating for R_2 changes from factors such as water content variation.¹⁸ The sensitivity of R_2' to concentration of deoxyhemoglobin has been reported by several studies^{19,20} and has been shown to correlate with the hypoxic state of tissue.²¹ Although R_2' does not allow for a direct measurement of OEF, previous studies have demonstrated that OEF is proportional to R_2' , after normalization to relative blood volume fraction and static dephasing, which is expected for protons in blood at the specific magnetic field strength.²²⁻²⁵ Additionally, this approach has been used previously to explore oxygen metabolism in brain tumors^{24,26} as well as stroke.²⁰ However, although higher measures of R_2' may suggest higher concentration of deoxyhemoglobin, OEF, and/or local hypoxia, many other biological and/or technical influences (e.g., B_1 homogeneity) may influence this measurement.

In the current study, we introduce a new technique for obtaining fast, whole-brain, noninvasive, high-resolution pH-sensitive and oxygen-sensitive MR imaging contrast using multi-echo amine proton CEST echo spin-and-gradient echo (SAGE) EPI (CEST-SAGE-EPI) on a clinical 3T MRI system. pH-weighted image sensitivity was obtained through quantification of the z -spectral asymmetry in the magnetic

transfer ratio (MTR) after selective saturation of the longitudinal magnetization of amine protons on glutamine at 3.0 ppm (MTR_{asym} at 3.0 ppm), whereas oxygen sensitivity was obtained through quantification of R_2' using a multi-echo SAGE-EPI readout to quantify relaxation rates R_2 and R_2^* . Sensitivity and accuracy of this approach were confirmed using custom phantoms containing both gadolinium diethylenetriamine penta-acetic acid (Gd-DTPA) and glutamine and different concentrations and pH. Finally, both MTR_{asym} at 3.0 ppm and R_2' for tumor and normal tissue were characterized in patients harboring diffuse or malignant gliomas.

2 | THEORY

2.1 | pH-sensitive and oxygen-sensitive MR contrast using multi-echo amine proton CEST-SAGE-EPI

The magnetization of bulk water protons undergoing chemical exchange with amine protons can be described by the Bloch-McConnell equations²⁷ in the form of

$$\frac{d\mathbf{M}(t)}{dt} = \mathbf{X} \cdot \mathbf{M}(t) - \mathbf{c}, \quad (1)$$

where

$$\mathbf{M} = \begin{pmatrix} M_{ax} \\ M_{bx} \\ M_{ay} \\ M_{by} \\ M_{az} \\ M_{bz} \end{pmatrix}, \mathbf{X} = \begin{pmatrix} C_{2a} & k_b & -\delta a & 0 & 0 & 0 \\ k_a & C_{2b} & 0 & -\delta b & 0 & 0 \\ \delta a & 0 & C_{2a} & k_b & -\omega_1 & 0 \\ 0 & \delta b & k_a & C_{2b} & 0 & -\omega_1 \\ 0 & 0 & \omega_1 & 0 & C_{1a} & k_b \\ 0 & 0 & 0 & \omega_1 & k_a & C_{1b} \end{pmatrix}, \mathbf{c} = \begin{pmatrix} 0 \\ 0 \\ 0 \\ 0 \\ M_{az0}/T_{1a} \\ M_{bz0}/T_{1b} \end{pmatrix}, \quad (2)$$

where pool a and pool b are the bulk water protons and amine protons, respectively; M_{az0} and M_{bz0} are the equilibrium magnetizations of pool a and pool b , respectively; k_b is the exchange rate of protons from pool b to pool a ; k_a is the exchange rate of protons from pool a to pool b as given by $(M_{b0}/M_{a0}) \cdot k_b$; ω_1 is the RF pulse amplitude as given by $\omega_1 = \gamma B_1(t)$, where γ is the gyromagnetic ratio and $B_1(t)$ is given in μT ; $\delta_a = \omega - \omega_a$ and $\delta_b = \omega - \omega_b$, where ω is the applied RF irradiation frequency, ω_a is the bulk water resonance frequency, and ω_b is the amine proton resonance frequency; T_{1a} and T_{1b} are the longitudinal relaxation times of pool a and pool b , respectively; and $C_{1a} = (1/T_{1a}) + k_a$, $C_{2a} = (1/T_{2a}) + k_a$, $C_{1b} = (1/T_{1b}) + k_b$, and $C_{2b} = (1/T_{2b}) + k_b$ represent the sum of exchange and relaxation rates. Equation 1 can be solved analytically to yield

$$\mathbf{M}(t) = e^{\mathbf{X}t} \cdot \mathbf{M}_0(\mathbf{X}/\mathbf{c}) - (\mathbf{X}/\mathbf{c}), \quad (3)$$

where $M_{az}(t)$ represents the longitudinal magnetization of bulk water available for subsequent readout after CEST effects. Assuming the spoiler duration and water excitation pulse duration are negligible, $M_{az}(t)$ immediately following excitation reflects the available longitudinal magnetization for subsequent readout. The chemical exchange between amine protons and bulk water protons can be characterized as a base-catalyzed process, governed by pH as follows:

$$k_b = k_0 + k_{\text{base}} * 10^{-(14-pH)} \quad (4)$$

where k_0 is the default exchange rate; k_{base} is the base-catalyzed rate constant; and k_b is the exchange rate of protons from the metabolite proton pool to the water pool.²⁸ In

glutamine phantoms with concentration of 50 mM, k_0 and k_{base} have been estimated to be 76 and 5.6 Hz, respectively.¹⁶

During the CEST imaging experiment, the RF saturation frequency ω is swept over a range of values to obtain a z -spectral data set.²⁹ To reduce the effects of T_1 and T_2 weighting, along with other confounding effects, the attenuation of bulk water magnetization following a saturation pulse is described by the MTR given by

$$MTR(\omega) = \frac{S(\omega)}{S_0} \quad (5)$$

where $S(\omega)$ is the amount of bulk water signal available after the saturation pulse with frequency ω ; and S_0 is the signal available without application of RF saturation. Because MTR can be affected by symmetric effects of direct water saturation and conventional magnetization transfer effects, CEST contrast is often described by the asymmetry in the

magnetization transfer ratio (MTR_{asym}) with respect to water proton resonance, as follows:

$$MTR_{\text{asym}}(\omega) = \frac{S(-\omega) - S(\omega)}{S_0}. \quad (6)$$

For amine proton CEST imaging, MTR_{asym} is evaluated at 3.0 ppm with respect to the bulk water resonance frequency.

Estimates of R'_2 were achieved through use of a SAGE-EPI readout consisting of 2 gradient echoes (TE_1 and TE_2), an asymmetric spin echo (TE_3), and a spin-echo (TE_4) EPI acquisition during a single excitation event (Figure 2). The solutions for R_2^* and R_2 using the SAGE EPI were eloquently described by Schmiedeskamp et al³⁰ as

$$A = Y^{-1}S, \quad (7)$$

where

$$S = \begin{pmatrix} \ln(S_1) \\ \ln(S_2) \\ \ln(S_3) \\ \ln(S_4) \end{pmatrix}, Y = \begin{pmatrix} 1 & 0 & -TE_1 & 0 \\ 1 & 0 & -TE_2 & 0 \\ 1 & -1 & -TE_4 + TE_3 & TE_4 - 2 \cdot TE_3 \\ 1 & -1 & 0 & -TE_4 \end{pmatrix}, A = \begin{pmatrix} \ln(S_0) \\ \ln(\delta) \\ R_2^* \\ R_2 \end{pmatrix}, \quad (8)$$

where S_n is the signal magnitude for the n th echo and δ is the differences in residual signal differences caused by imperfectly matched slice profiles between echo trains before and after the refocusing pulse.³¹ Finally, the reversible transverse relaxation rate, R'_2 , is calculated as

$$R'_2 = R_2^* - R_2. \quad (9)$$

3 | METHODS

3.1 | Amine proton CEST-SAGE-EPI

Simultaneous acquisition of pH-sensitive information and relaxometry measures of R'_2 were performed through modification of a previously described CEST-EPI sequence¹⁶ to include a SAGE-EPI readout (Figure 2). The SAGE-EPI readout consisted of 2 gradient echoes ($TE_1 = 14.0$ ms; $TE_2 = 34.1$ ms), an asymmetric spin echo ($TE_3 = 58.0$ ms), and a spin echo ($TE_4 = 92.4$ ms). All phantom and human CEST-SAGE-EPI data were acquired with a CEST saturation pulse train consisting of 3 ($3 \times$) 100-ms Gaussian pulses with amplitude $B_1 = 6 \mu\text{T}$, $TR > 10\,000$ ms, $FOV = 240 \times 217$, matrix size = 128×104 , partial Fourier encoding = 6/8, GRAPPA = 3, bandwidth = 1630 Hz/pixel, and 25 contiguous slices with a 4-mm slice thickness. A total of 29 z -spectral points were acquired with data around ± 3.0 ppm and 0.0 ppm with respect to water (from -3.5 to

-2.5 in intervals of 0.1; from -0.3 to $+0.3$ in intervals of 0.1; and from $+2.5$ to $+3.5$ in intervals of 0.1). An additional reference S_0 scan with identical parameters and no saturation pulse was acquired with number of excitations or averages = 4. The total acquisition time for CEST-SAGE-EPI was 7 minutes and 30 seconds, benchmarked on a 3T Siemens Prisma MR scanner (Software Versions VE11A-C; Siemens Healthcare, Erlangen, Germany).

3.2 | Phantom testing

To demonstrate the ability to simultaneously acquire pH-sensitive information along with relaxometry measures of R_2 , R_2^* , and R'_2 , we performed CEST-SAGE-EPI, multi-echo gradient-echo (ME-GRE), and multi-echo spin-echo (Carr-Purcell-Meiboom-Gill [CPMG]) MR acquisition in a series of 36 glutamine phantoms (100 mM) with combinations of varying pH (5.0, 5.5, 6.0, 6.5, 7.0, 7.5) and gadopentetic acid (Gd-DTPA; Magnevist, Bayer HealthCare Pharmaceuticals, Berlin, Germany) concentration (0, 0.25, 0.5, 1.0, 1.5, and 2.0 mM) in 50-mL falcon tubes. The 100-mM glutamine solution was prepared first using distilled water. The pH in each phantom was titrated using dilute acid (0.1N HCl) and base (0.1N NaOH) solution. The desired Gd-DTPA was then added to the phantom solution and vortexed. All samples were vortexed and pH was re-evaluated prior to MRI acquisition. The ME-GRE sequence used for R_2^* quantitation was

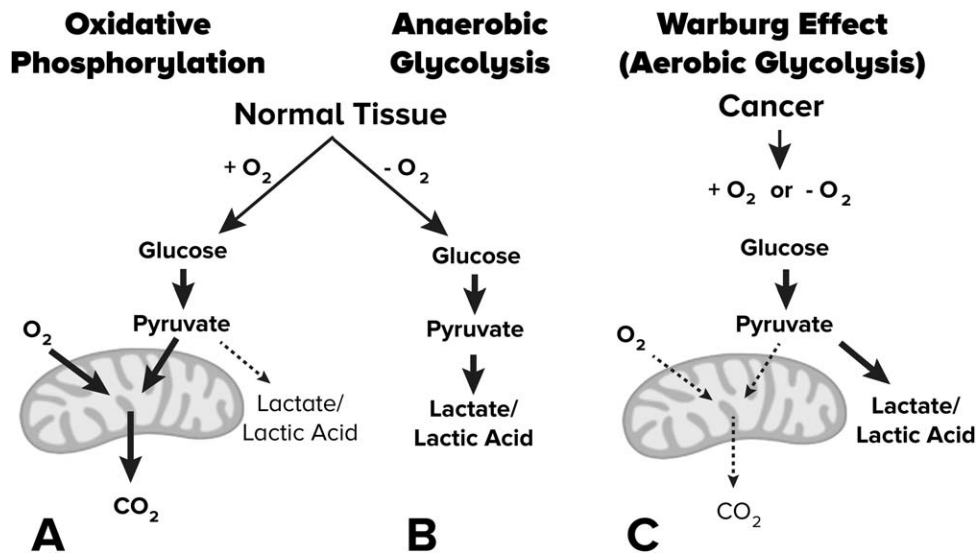


FIGURE 1 The Warburg effect. A, Within normal tissues in the presence of oxygen, glucose is converted to pyruvate and then used for oxidative phosphorylation within the mitochondria. B, In normal tissues within a hypoxic environment, glucose is converted to pyruvate, then to lactate or lactic acid, decreasing extracellular pH. C, In cancer cells, glucose is converted to pyruvate then to lactate and lactic acid (80-85%) and a small portion of pyruvate enters the citric acid cycle (5-15%), regardless of whether oxygen is present. This altered metabolism, also known as the Warburg effect or aerobic glycolysis, results in increased extracellular acidity (lower pH) even when tumor tissue is well perfused

collected with TE = 20/40/60/80 ms, TR = 10 000 ms, flip angle = 90°, FOV = 217 × 240 mm, matrix size = 116 × 128, slice thickness = 4 mm, and pixel bandwidth = 260 Hz. The CPMG sequence used for R₂ quantitation was performed with TE = 49/98/147/196/245/294/343/392 ms, TR = 10 000 ms, flip angle = 90°, FOV = 217 × 240 mm, matrix size = 116 × 128, slice thickness = 4 mm, and pixel bandwidth = 260 Hz. Both the ME-GRE and CPMG sequences were repeated to improve SNR. All phantom experiments were physically repeated twice to ensure repeatability and compared with theoretical values using Bloch-McConnell simulations. Contrast-to-noise ratio (CNR) of MTR_{asym} at 3 ppm between any 2 samples of differing pH *a* and *b* was calculated as

$$CNR = \frac{|\mu_a - \mu_b|}{\left(\frac{\sigma_a^2 - \sigma_b^2}{2}\right)^2}. \quad (10)$$

3.3 | Patients

A total of 47 histologically proven glioma patients (World Health Organization [WHO] IV, *n* = 20; WHO III, *n* = 14; WHO II, *n* = 13) were enrolled in the current study prior to initial surgical resection or at first recurrence. All patients provided informed, written consent to have advanced imaging, and this information included in our internal review board–approved research database. Patient characteristics are outlined in Table 1. In addition to CEST-SAGE-EPI prior to

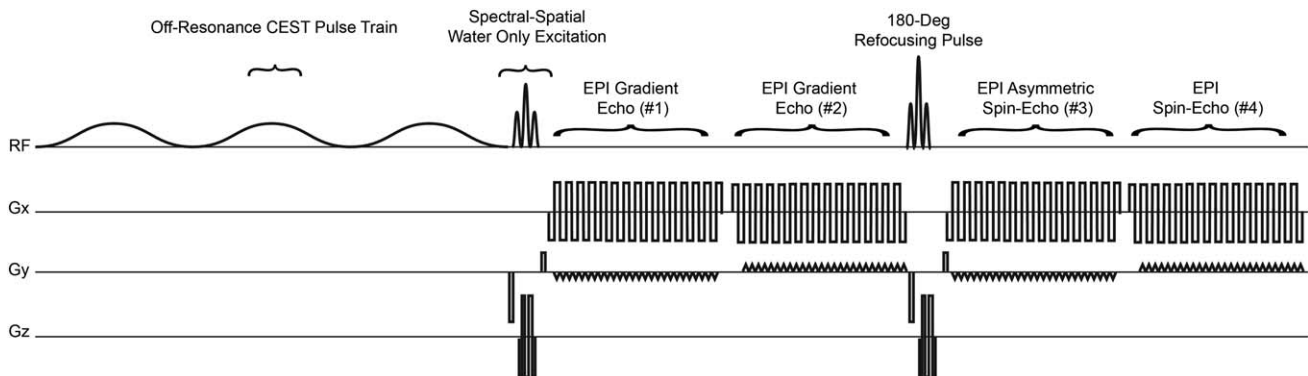


FIGURE 2 Pulse sequence diagram for a multi-echo amine CEST spin-and-gradient echo (SAGE EPI (CEST-SAGE-EPI) sequence. After nonselective off-resonance CEST excitation consisting of 3 100-ms Gaussian pulses, a spectral-spatial water-only excitation pulse is invoked. Following excitation, 2 gradient-echo EPI trains are acquired (echoes 1 and 2), followed by a 180° refocusing pulse. Finally, an asymmetric spin-echo EPI train (echo 3) and a standard spin-echo EPI train (echo 4) are acquired. Partial Fourier k-space acquisition strategies were used to further reduce TEs (e.g., TE₁/TE₂/TE₃/TE₄ = 14.0/34.1/58.0/92.4 ms for the current study)

TABLE 1 Patient demographics

Patient No.	Age	Sex	2016 WHO grade	IDH status	2016 WHO diagnosis	New or recurrent
1	60	M	4	WT	GBM	New
2	62	M	4	WT	GBM	New
3	53	F	4	WT	GBM	New
4	49	M	4	WT	GBM	New
5	60	M	4	WT	GBM	New
6	46	F	4	MUT	GBM	Recurrent
7	53	F	4	WT	GBM	Recurrent
8	76	F	4	WT	GBM	Recurrent
9	55	F	4	WT	GBM	Recurrent
10	59	M	4	WT	GBM	Recurrent
11	60	M	4	WT	GBM	Recurrent
12	45	M	4	WT	GBM	Recurrent
13	48	F	4	WT	GBM	Recurrent
14	66	M	4	WT	GBM	Recurrent
15	53	F	4	WT	GBM	Recurrent
16	75	M	4	WT	GBM	Recurrent
17	56	M	4	WT	GBM	Recurrent
18	62	M	4	WT	GBM	Recurrent
19	75	M	4	WT	GBM	Recurrent
20	60	M	4	WT	GBM	Recurrent
21	29	F	3	MUT	AA	New
22	51	M	3	MUT	AA	New
23	64	F	3	WT	AA	New
24	56	M	3	WT	AA	New
25	62	M	3	WT	AA	New
26	69	M	3	WT	AA	New
27	36	F	3	MUT	AO	New
28	29	M	3	MUT	AO	New
29	82	M	3	WT	AA	Recurrent
30	71	F	3	WT	AA	Recurrent
31	47	F	3	WT	AA	Recurrent
32	76	F	3	WT	AA	Recurrent
33	66	M	3	MUT	AO	Recurrent

(Continues)

TABLE 1 (Continued)

Patient No.	Age	Sex	2016 WHO grade	IDH status	2016 WHO diagnosis	New or recurrent
34	38	F	3	MUT	AO	Recurrent
35	38	M	2	MUT	A	New
36	41	M	2	MUT	A	New
37	29	F	2	MUT	A	New
38	30	F	2	MUT	A	New
39	22	M	2	MUT	A	New
40	48	M	2	WT	A	New
41	87	F	2	WT	A	New
42	41	M	2	MUT	O	New
43	42	F	2	MUT	A	Recurrent
44	36	F	2	MUT	A	Recurrent
45	73	M	2	WT	A	Recurrent
46	41	F	2	MUT	O	Recurrent
47	91	M	2	WT	O	Recurrent

Note: M, male; F, female; MUT, mutant; WT, wild type; A, astrocytoma; O, oligodendroglioma; AA, anaplastic astrocytoma; AO, anaplastic oligodendroglioma.

contrast administration, all patients received the anatomic images according to the standardized brain tumor imaging protocol,³² including T₂-weighted fluid-attenuated inversion recovery (FLAIR) images, T₂-weighted turbo spin-echo images, and diffusion-weighted images with 3-mm slice thickness and no interslice gap, along with parameter-matched, 1-mm isotropic 3D T₁-weighted MPRAGE scans before and following injection of 0.01 mg/kg Gd-DTPA.

3.4 | Postprocessing

Clinical postprocessing of CEST-SAGE-EPI consisted of affine motion correction (mcflirt; FSL, FMRIB, Oxford, United Kingdom) and B₀ correction via the WASSR (water saturation shift referencing) method,³³ and/or creating B₀ maps using phase information from the 2 acquired gradient echoes (Supporting Information Figure S1). An integral of width of 0.4 ppm was then taken around both the −3.0 and +3.0 ppm (−3.2 to −2.8 and +2.8 to +3.2, respectively) spectral points of the inhomogeneity-corrected data. These data points were combined with the S₀ image to calculate MTR_{asym} at 3.0 ppm as defined by Equation 5. Estimates of T₂^{*}, T₂, T₂['], R₂['], R₂, and R₂['] from ME-GRE or CPMG were obtained by performing a mono-exponential fit to the gradient and spin echoes, respectively, whereas estimates of the same parameters were obtained using Equation 8. Maps of R₂['] were then calculated as

$$R_2' = R_2^* - R_2 = \frac{1}{T_2'} - \frac{1}{T_2^*} - \frac{1}{T_2} \quad (11)$$

with a higher value of R₂['] suggesting relatively higher concentration of hemoglobin, oxygen extraction fraction, and/or hypoxia.²²⁻²⁶

3.5 | Data analysis

For all data, the average MTR_{asym} at 3.0 ppm calculated from the first (TE = 14.0 ms) and second (TE = 34.1 ms) gradient echoes were averaged to decrease increase the SNR of the resulting MTR_{asym} images. The 2 gradient echoes were chosen instead of all echoes due to slightly higher variability in MTR_{asym} measurements from asymmetric spin-echo and spin-echo measurements, due to the longer TE and additional signal loss from transverse relaxation. In phantom samples, regions of interest were drawn within each sample and the mean (μ) and SD (σ) of MTR_{asym} at 3 ppm for voxels within the sample were calculated.

When evaluating glioma patients, volumes of interest were drawn within normal-appearing white matter (NAWM) contralateral to the hemisphere containing evidence of tumor on T₂-weighted FLAIR images. Lesions exhibiting abnormal T₂ hyperintensity on FLAIR images (“T₂ lesions” volumes of interest) were manually contoured on all patients. To reduce the influence of outliers, the median and median absolute deviation of MTR_{asym} and R₂['] within these regions

were calculated, and the median absolute deviation was used to define variability for all measurements. A Wilcoxon signed-rank test was used to determine whether averaging MTR_{asym} from 2 gradient echoes resulted in a decrease in healthy-tissue MTR_{asym} variability compared with a single gradient echo. For glioblastoma patients, volumes of interest of gadolinium contrast enhancement (CE) were segmented using T_1 subtraction maps and a semi-automated thresholding method outlined previously.^{34,35} Regions of central necrosis were also delineated and examined. A paired t-test was used to determine whether R_2' and MTR_{asym} differed between T_2 -hyperintense lesions and NAWM. Within glioblastoma patients (WHO grade IV), a one-way repeated-measures analysis of variance (ANOVA) and Tukey's test for multiple comparisons was used to determine whether R_2' or MTR_{asym} at 3 ppm differed among regions of NAWM, T_2 hyperintense lesions, regions of CE, and areas of central necrosis. An additional one-way ANOVA and Tukey's test for multiple comparisons was used to compare R_2' or MTR_{asym} at 3 ppm for T_2 lesions across glioma grades II, III, and IV.

4 | RESULTS

The value of MTR_{asym} at 3.0 ppm within each glutamine phantom, varying by pH, was similar across all 4 echoes, showing a characteristic increase in MTR_{asym} at 3.0 ppm with decreasing pH (Figure 3A; ANOVA, $p = .999$; comparison across echoes, $p > .99$). These experimental results closely matched the simulation results using measured and theoretical relaxation and exchange rates (Figure 3A). The CNR was higher when averaging measurements from the 2 gradient echoes ($TE = 14.1$ ms and 34.1 ms) compared with a single gradient echo ($TE = 14.1$ ms) in phantom samples containing the same concentration of glutamine, but varying pH. In particular, CNR was approximately 13% higher when comparing pH = 7.5 to 7.0 ($CNR_{1\&2} = 2.68$; $CNR_1 = 2.37$), 7% higher when comparing pH = 6.5 and 7.0 ($CNR_{1\&2} = 5.07$; $CNR_1 = 4.74$), 15% higher when comparing pH = 6.0 versus 7.0 ($CNR_{1\&2} = 17.2$; $CNR_1 = 15.0$), and 6.5% higher when comparing pH = 6.0 versus 6.5 ($CNR_{1\&2} = 6.72$; $CNR_1 = 6.31$). Consistent with phantom results, the median MTR_{asym} at 3.0 ppm in NAWM across all patients was not significantly different when using a single echo and the average of 2 gradient echoes ($p = .31$); however, the median absolute deviation, a measure of variance in the measurements, was significantly lower when averaging the 2 gradient echoes ($p = .003$).

In phantom samples containing varying concentration of Gd-DTPA, CEST-SAGE-EPI estimates of R_2 , R_2^* , and R_2' varied linearly with concentration (Figure 3B), with estimates of transverse relaxivities of $R_2 = 6.24 \pm 0.04 \text{ mM}^{-1} \cdot \text{sec}^{-1}$

($p < .0001$), $R_2^* = 6.86 \pm 0.10 \text{ mM}^{-1} \cdot \text{sec}^{-1}$ ($p < .0001$), and $R_2' = 0.61 \pm 0.08 \text{ mM}^{-1} \cdot \text{sec}^{-1}$ ($p = .0007$). Phantom results identified a strong, significant linear correlation between R_2 measurements using CEST-SAGE-EPI and CPMG (Figure 3C; $R^2 = 0.9943$, $p < .0001$) and did not differ by pH ($p = .9915$). Estimates of R_2 using CEST-SAGE-EPI, however, were lower than estimates of R_2 using standard CPMG measurements (slope = 0.8845 ± 0.006 , $p < .0001$ compared with slope = 1), with CEST-SAGE-EPI estimates approximately 760 μs lower on average than CPMG measurements ($\sim 7.1\%$). A strong linear correlation was also observed between R_2^* measurements obtained using CEST-SAGE-EPI and ME-GRE measurements (Figure 3D; $R^2 = 0.9727$, $p < .0001$), and these measurements also did not differ by pH ($p = .2184$). Estimates of R_2^* were not significantly different from measurements obtained using standard ME-GRE measurements (slope = 0.9862 ± 0.0155 , $p = .3819$, showing no difference between slope = 1). Consistent with these results, calculated estimates of R_2' obtained through subtraction of sequential CPMG and ME-GRE measurements were congruent with SAGE-EPI measurements (Figure 3E; slope = 1.26 ± 0.1301 , $p = .0555$, showing no difference between slope = 1) and did not differ by pH ($p = .0533$).

Although measurements of transverse relaxation rate were not affected by pH, the relationship between MTR_{asym} at 3.0 ppm and pH was affected by transverse relaxation rate (Figure 3F). Specifically, as transverse relaxation rates R_2 or R_2^* increased as a result of increased concentration of Gd-DTPA, the sensitivity of MTR_{asym} at 3.0 ppm to acidic pH decreased, particularly when concentrations were higher than 1 mM, corresponding to T_2 measurements of 150 to 170 ms and $T_2^* = 130$ to 170 ms. Repeated experiments showed higher coefficient of variation with higher concentrations of Gd-DTPA, or lower T_1 , as well as higher coefficient of variation with higher pH (Figure 3G).

Qualitatively, the T_2 hyperintense lesions in all patients exhibited heterogeneous areas of both elevated MTR_{asym} at 3.0 ppm (acidity) and R_2' (hypoxia). Many areas of nonenhancing tumor in all patients exhibited uncharacteristically low measures of R_2' despite evidence of elevated acidity, suggesting nonenhancing tumor regions may be adequately oxygenated and undergoing aerobic glycolysis (Figure 1C). For example, Figure 4A illustrates a WHO grade II astrocytoma with an area of moderately elevated acidity in the medial frontal lobe; however, this region exhibited R_2' approximately 50% lower than surrounding NAWM. Figure 4B illustrates a large nonenhancing, isocitrate dehydrogenase (IDH) mutant WHO grade III astrocytoma with sizeable regions of macroscopic necrosis, as illustrated by T_1 hypointensity. These areas of necrotic tissue exhibited both high levels of acidity and hypoxia, whereas the surrounding nonenhancing components with largely intact blood-brain barrier had elevated acidity, as suggested by higher MTR_{asym} at

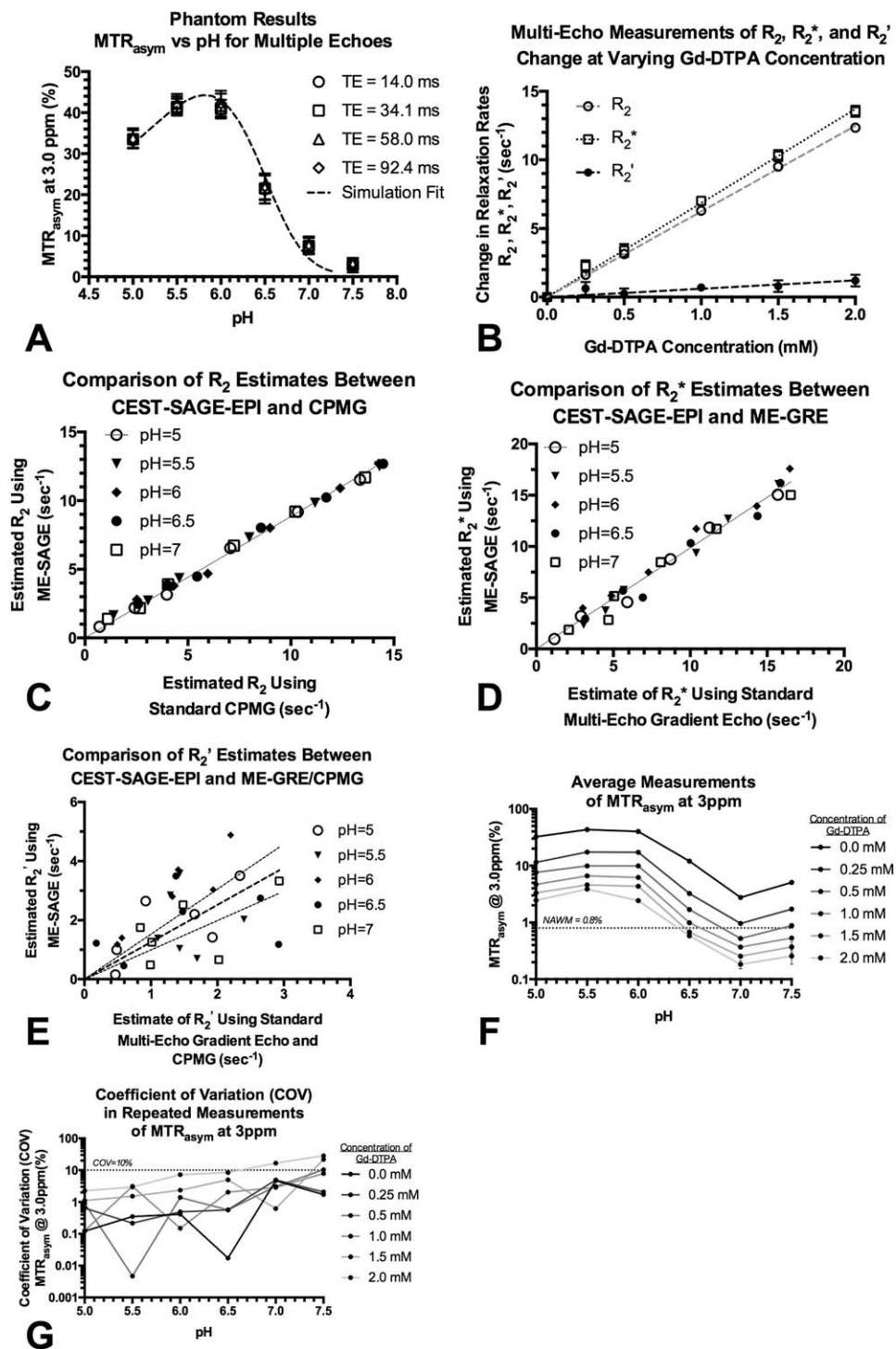


FIGURE 3 Simulation and phantom testing. A, The CEST contrast increases with decreasing pH within a physiological pH range similarly for all 4 echoes in an amino acid phantom and simulation estimates. These measurements closely match simulation estimates with measured or estimated relaxation and exchange rates (dashed lines). B, R_2 and R_2^* as measured by the multi-echo sequence show a linear increase with increasing gadolinium diethylenetriamine penta-acetic acid (Gd-DTPA) concentration. Estimates of $R_2 = 6.24 \pm 0.04 \text{ mM}^{-1} \cdot \text{sec}^{-1}$, $R_2^* = 6.86 \pm 0.10 \text{ mM}^{-1} \cdot \text{sec}^{-1}$, and $R_2' = 0.61 \pm 0.08 \text{ mM}^{-1} \cdot \text{sec}^{-1}$. C, Comparison between measured R_2 using CEST-SAGE-EPI and Carr-Purcell-Meiboom-Gill (CPMG) show strong correlation ($R^2 = 0.9943$, $p < .0001$), independent of pH ($p = .9915$). D, Comparison between measured R_2^* using CEST-SAGE-EPI and multi-echo gradient echo (ME-GRE) show a strong correlation ($R^2 = 0.9727$, $p < .0001$) and no dependence on pH ($p = 0.2184$). E, Estimates of R_2' obtained through subtraction of sequential CPMG and ME-GRE measurements were not significantly different from those obtained using multi-echo SAGE EPI (slope = 1.26 ± 0.1301 , $p = .0555$) and did not differ by pH ($p = 0.0533$). F, Amine CEST has decreased sensitivity in the presence of contrast agents (Gd-DTPA) that shorten T_1 and T_2 . Thus, edematous tumor tissue with longer T_1 and T_2 have higher CEST contrast in acidic environments. G, Coefficient of variation measured from multiple test-retest experiments is also higher in the presence of contrast agents or in environments with shorter T_1 and T_2 characteristics. MTR_{asym}, magnetization transfer ratio asymmetry

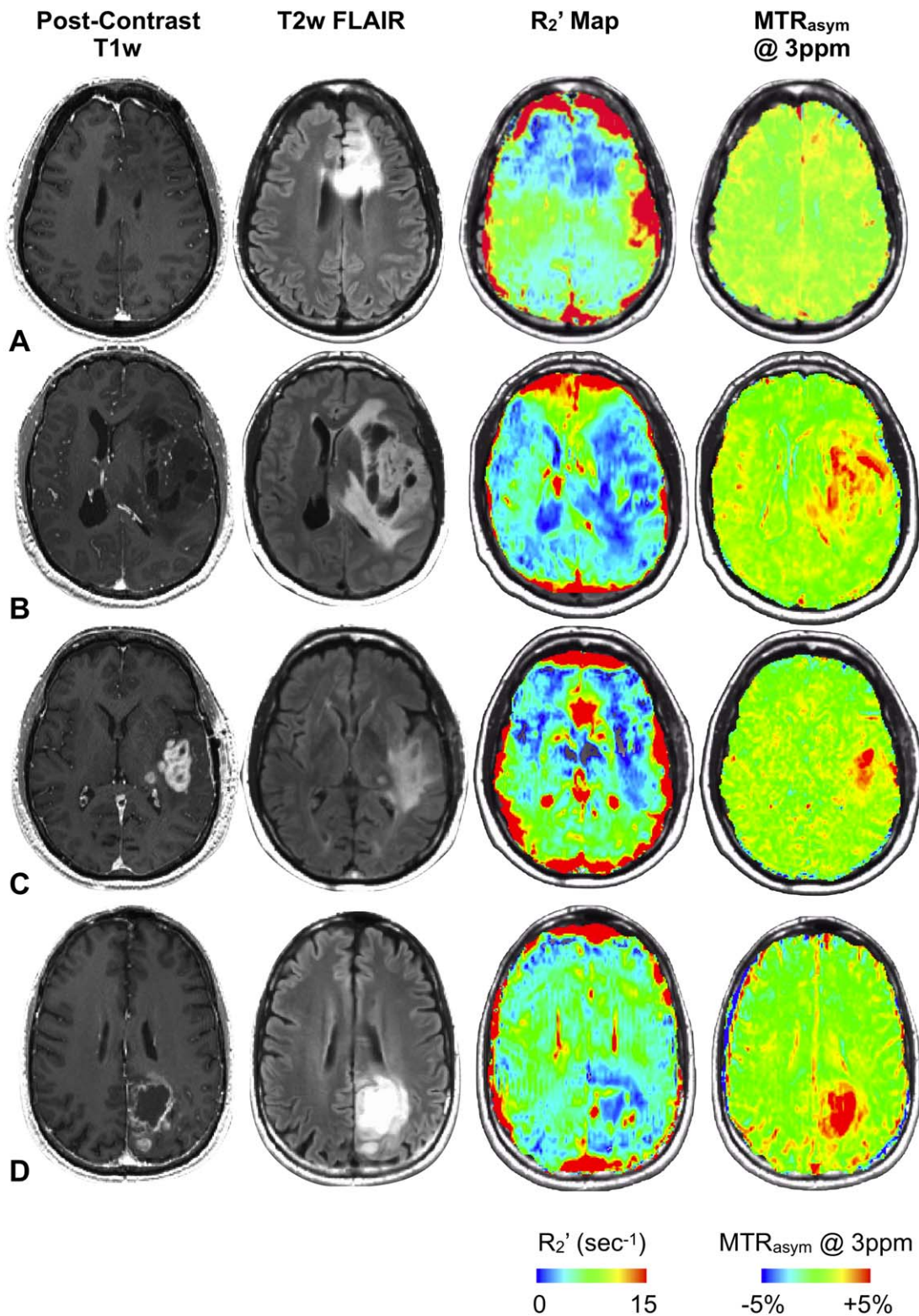


FIGURE 4 pH-sensitive and oxygen-sensitive MR images of human gliomas. A, A 42-year-old female with a nonenhancing recurrent World Health Organization (WHO) II isocitrate dehydrogenase (IDH) mutant astrocytoma (patient #43) exhibiting a region of focal acidity (high MTR_{asym} at 3 ppm) and low oxygen consumption (low R₂'). B, A 51-year-old male patient with a newly diagnosed nonenhancing IDH mutant WHO III anaplastic astrocytoma (patient #22). This lesion showed large, heterogeneous regions of abnormally high and low hypoxia and acidity. C, A 53-year-old female patient with a recurrent IDH wild-type WHO IV glioblastoma exhibiting a region of focal acidity and large regions of low oxygen consumption (patient #15). D, A 53-year-old female with a newly diagnosed IDH wild-type WHO IV glioblastoma (patient #3) displaying ring enhancement, central necrosis, elevated acidity, and oxygen extraction (hypoxia) within the enhancing region as well as low oxygen consumption in surrounding nonenhancing tumor. T_{1w}, T₁-weighted image; T_{2w}, T₂-weighted image; FLAIR, fluid-attenuated inversion recovery

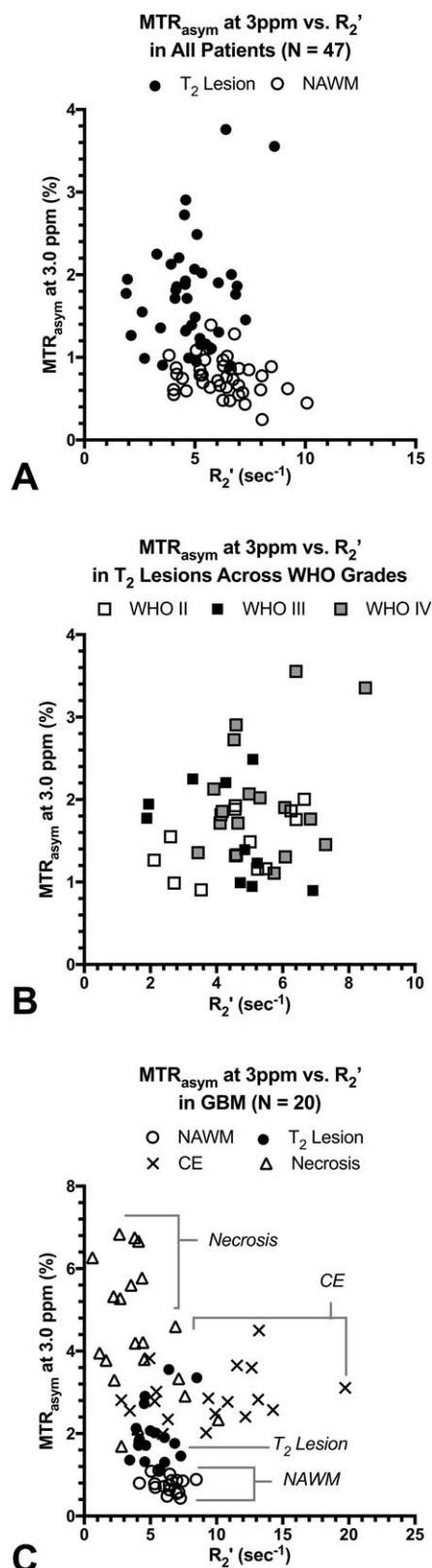


FIGURE 6 Combined pH-sensitive and oxygen-sensitive MR measurements in human gliomas illustrating additional separation of tissue types. A, Value of MTR_{asym} at 3 ppm (%) versus R₂' for NAWM and T₂ hyperintense lesions in all patients pooled across tumor grades. B, Value of MTR_{asym} at 3 ppm (%) versus R₂' in T₂ hyperintense regions for different tumor grades. C, Value of MTR_{asym} at 3 ppm (%) versus R₂' in different tissue types in GBM

Median MTR_{asym} at 3.0 ppm within T₂ hyperintense lesions ($1.7 \pm 0.1\%$) were significantly higher than NAWM ($0.8 \pm 0.03\%$) when pooling all patients across grade (Figure 5D; paired t-test, $p < .0001$). Within T₂ hyperintense lesions, the median MTR_{asym} at 3.0 ppm was significantly different across tumor grade (Figure 5E; ANOVA, $p = .0297$), with WHO IV glioblastoma ($2.0 \pm 0.2\%$) exhibiting significantly higher acidity compared with WHO II gliomas ($1.5 \pm 0.1\%$; Tukey's test, adjusted $p = .0432$). No difference was observed between WHO III gliomas ($1.6 \pm 0.2\%$) compared with other grades (adjusted $p > .05$). In a separate comparison, IDH mutant gliomas exhibited a slightly higher degree of tumor acidity compared with IDH wild-type tumors when correcting for grade (adjusted $p = .0434$). Within WHO IV glioblastoma, significant differences in median MTR_{asym} at 3.0 ppm were observed among various tissue types (Figure 5F; ANOVA, $p < .0001$). Areas of macroscopic necrosis exhibited the highest MTR_{asym} at 3.0 ppm degree of acidity (MTR_{asym} at 3.0 ppm = $4.4 \pm 0.4\%$) compared with all other tissue types, including CE lesions ($2.9 \pm 0.1\%$; Tukey's test, adjusted $p < .0001$), T₂ hyperintense regions ($2.0 \pm 0.2\%$, adjusted $p < .0001$), and NAWM ($0.8 \pm 0.04\%$, adjusted $p < .0001$). Additionally, CE tumor exhibited significantly higher median MTR_{asym} at 3.0 ppm compared with T₂ hyperintense lesions (Tukey's test, adjusted $p = .0218$) and NAWM (Tukey's test, adjusted $p < .0001$), whereas T₂ lesions showed higher median MTR_{asym} at 3.0 ppm (Tukey's test, adjusted $p < .0001$).

Examination of acidity and hypoxia characteristics within T₂ hyperintense lesions pooled across tumor grade were markedly different from NAWM (Figure 6A), as T₂ hyperintense lesions tended to be more acidic but slightly less hypoxic compared with NAWM. T₂ hyperintense lesions did not show substantial separation across tumor grade (Figure 6B). Glioblastoma exhibited distinct characteristics across various tissue components (Figure 6C), with NAWM and T₂ hyperintense lesions having relatively lower acidity and hypoxia combined with CE tumor and macroscopic necrotic tissue. The CE tumor exhibited a moderately high level of acidity, along with high degrees of oxygen extraction, whereas necrotic tissue showed low oxygen extraction yet high acidity.

5 | DISCUSSION

High-resolution pH-sensitive and oxygen-sensitive MR imaging contrast in brain tumors can be achieved on clinical 3T MR systems by implementing a multi-echo SAGE-EPI readout after off-resonance saturation or CEST preparation of amine protons (3.0 ppm). Comparable techniques for CEST imaging that take advantage of multiple echo readouts are relatively limited. Sun et al described a sequence that

uses a CPMG readout following CEST saturation for improving CNR in agarose phantoms by averaging images from a spin-echo train with TEs between 30 and 60 ms.³⁶ However, this sequence only measured R_2 characteristics and could not correct for B_0 using phase information available via multiple gradient echoes. The fast EPI readout available using CEST-SAGE-EPI vastly improves acquisition times over slower, single-slice, or volumetric approaches.³⁷⁻³⁹ Song et al⁴⁰ and others have described single-echo EPI approaches to speed up acquisition time; however, these studies lacked concurrent measurement of subsequent echoes that would allow for estimation of R_2 , R_2^* , R_2' and B_0 . Thus, CEST-SAGE-EPI has many advantages including speed, in-line B_0 mapping, whole-brain coverage, and simultaneous CEST, R_2 , R_2^* , and R_2' quantitation.

Mathematical simulations and phantom measurements confirmed the relationship between MTR_{asym} at 3.0 ppm and pH reported previously.¹⁶ Measurements of transverse relaxivity for Gd-DTPA were found to be $R_2 = 6.24 \pm 0.04 \text{ mM}^{-1} \cdot \text{sec}^{-1}$ and $R_2^* = 6.86 \pm 0.10 \text{ mM}^{-1} \cdot \text{sec}^{-1}$, which is consistent with the literature.^{41,42} Measurements of R_2 and R_2^* also did not vary as a function of pH. As compared with CPMG measurements, CEST-SAGE-EPI tended to underestimate R_2 , consequently resulting in overestimation of R_2' ; however, the magnitude of this difference averaged less than 1 ms (~ 760 us), or less than 10% difference, and increased with relaxation rate R_2 . This discrepancy may be related to inaccurate modeling of imperfections during RF inversion during SAGE-EPI readout, as has been suggested in previous SAGE-EPI studies.^{30,31} In addition to OEF, R_2' value may also be influenced by venous blood fraction as reported by several studies.²²⁻²⁵ A more direct quantification of oxygen consumption or comparison may be achieved with high-field ^{17}O MRI by detecting metabolically produced H_2^{17}O ,⁴³ or with ^{17}O MRS.⁴⁴

As demonstrated previously,¹⁶ edematous tissues and cancer tissues with long T_2 tend to amplify pH-dependent CEST contrast, whereas tissues with shorter T_2 exhibit only a few percentage changes in contrast, even in highly acidic and highly concentrated amino acid environments. In particular, with relatively short T_2/T_2^* , including normal appearing white and gray matter may not have suitable sensitivity or CNR to provide meaningful pH information. Thus, the current CEST-SAGE-EPI sequence may not be immediately useful to explore functional or metabolic changes in otherwise normal neural tissues without additional considerations (e.g., higher field strengths, more averages), but it is uniquely suited for detection and assessment of brain tumor or oncologic metabolism. Although MTR_{asym} contrast could be altered by effects from exchangeable proton pools other than amine protons, we have shown with phantoms (Supporting Information Figure S3) that the low pH results in elevation of MTR_{asym} at 3.0 ppm despite the presence of amide protons

and MT effect (introduced with 5% egg-white protein), and this is comparable to previous reports.¹⁶ The predominant pH dependence of MTR_{asym} at 3.0 ppm could be explained by the high irradiation amplitude ($B_1 = 6 \mu\text{T}$) preferably saturating fast-exchanging amine protons when compared with other proton pools. Another concern with using amine CEST contrast at 3.0 ppm is that it could suffer from an insufficient source of exchangeable protons if glutamine concentration is too low. In addition to glutamine, other amino acids and neurotransmitters possessing a similar amine functional group have similar pH dependence of exchange rate and MTR_{asym} at 3.0 ppm.¹⁶ Large molecules such as bovine serum albumin were also reported to show characteristics of fast-exchanging amine protons at 3.0 ppm.⁴⁵ With a total of about 20 to 25 mM amino acids within normal neural tissues⁴⁶ and other contributions of amine proton pools, sufficient amine CEST contrast within tumor tissues is highly probable.

Combined information about both median tissue acidity (MTR_{asym} at 3.0 ppm) and oxygen extraction (R_2') helped to further delineate various tissue types and provide additional insights into the tumor microenvironment. Consistent with tumor biology and the Warburg effect, we observed elevated acidity in tumor tissues even when there was adequate oxygen delivery due to an intact BBB, high neovascularity, and high blood flow. In particular, we observed lower levels of hypoxia and high acidity in regions of nonenhancing tumor (T_2/FLAIR hyperintensity) (Figure 5A,D; Figure 6A,C), which can have elevated vascularity depending on the degree of malignancy and/or grade. This was similar across tumor grade, although glioblastoma had slightly higher levels of hypoxia compared with lower grades. In the same tumors we observed substantially higher levels of hypoxia in areas of CE (Figure 4D; Figure 5C; Figure 6A,C), which is known to be the most aggressive⁴⁷ and hypoxic.⁴⁸⁻⁵⁰ These data suggest that tumor acidity and oxygen consumption are both complex and spatially heterogeneous, consistent with the known genetic, histopathologic, proteomic, and metabolic spatial heterogeneity.^{51,52} Hypoxic, nonhypoxic, and/or acidic tumors may also have differing therapeutic responses, as tumor hypoxia and acidity are both known to reduce sensitivity to chemoradiation. Thus, a tool that can colocalize areas of simultaneous pH and oxygen imbalance may allow for future therapeutic strategies to include radiation boost to regions containing the most hypoxic and acidic environments. Additionally, this tool may also allow for evaluation of direct inhibition of energetic pathways as a therapeutic target in these tumors.⁵³⁻⁵⁵

In addition to tissue acidity and reduced oxygen consumption, the Warburg effect is also characterized by altered levels of glucose consumption. Dynamic glucose-enhanced MRI, which selectively saturates hydroxyl protons of glucose and allows for a dynamic detection of CEST contrast during glucose uptake, has shown promising results in mapping in

animals^{56,57} and in human tumor patients⁵⁸⁻⁶⁰ and could potentially add another important piece of information about the tumor microenvironment.

Mutations of isocitrate dehydrogenase (IDH1) are common in less aggressive gliomas and cause inhibition of the conversion of isocitrate to alpha-ketoglutarate, resulting in a buildup of 2-hydroxyglutarate (2HG), inhibiting oxidative phosphorylation and therefore inhibiting the ability of cells to use aerobic glycolysis.⁶¹ Therefore, we hypothesized that IDH1-mutated tumors may have lower R_2' measurements compared with IDH1 wild-type tumors, consistent with previous work by Stadbauer et al.⁶² Although we observed slightly lower R_2' in IDH1 mutated patients compared with wild-type patients, these effects were not statistically significant. Further studies in a larger patient cohort are needed to better understand this relationship and whether pH-sensitive and oxygen-sensitive MR signatures can identify IDH1 mutant tumors.

One potential limitation of our approach is using the conventional asymmetric analysis (MTR_{asym}) to interpret CEST effects. Although the MTR_{asym} approach removes the symmetric effects from direct water saturation, the resulting contrast is still influenced by a number of other effects, including asymmetric magnetic transfer effect of semisolid tissue components,⁶³ nuclear Overhauser enhancement 0 to 5 ppm upfield to water proton resonance frequency,⁶⁴ and mixing effects from nearby exchangeable proton pools. Several alternative approaches have been developed to mitigate these problems, including chemical exchange rotation transfer,⁶⁵ Lorentzian difference analysis,⁴⁵ multiple-pool Lorentzian fit,^{66,67} and the 3-point method.⁶⁸ Further investigation of pH-sensitive and oxygen-sensitive imaging with CEST-SAGE-EPI sequence could potentially benefit from applying these methods.

Additionally, proton exchange rates are influenced by temperature, with faster exchange rates of amine protons observed at higher temperatures, due to increased kinetic energy along with increased T_2 relaxation times resulting in increased available NMR signal at a given frequency. Thus, phantom results at room temperature ($\sim 18^\circ\text{C}$) in the current studies are likely to underestimate MTR_{asym} when compared with in vivo comparisons ($\sim 37^\circ\text{C}$), as has been previously demonstrated.¹⁶ Thus, care should be given when interpreting absolute values of MTR_{asym} observed in the phantom portion of the current study.

In vivo R_2' mapping using SAGE-EPI readout can be influenced by a variety of technical issues, however, including B_1 inhomogeneity or mismatch between excitation and refocusing slice profiles, as well as biological factors including the effects of water diffusion and multiple water compartments within the tissues.^{31,69} The CEST contrast may also be influenced by multiple water compartments within tissues, although the water signal is thought to be predominantly

from the extracellular water pool due to the very short relaxation times of bound intracellular water.⁷⁰

Technical imperfections including static magnetic field (B_0) and transmit RF field (B_1) inhomogeneity may also have led to altered image contrast. In our study, B_0 inhomogeneity was corrected with B_0 map generated from the WASSR method or from multi-echo B_0 mapping; however, B_1 inhomogeneities were not compensated for. B_1 inhomogeneity under 3T is reported to be relatively small (deviation < 10 to 20%) and have limited effect on T_2 quantification⁷¹ and pH-sensitive CEST contrast¹⁶ within the variation range in the current study. Nevertheless, validation of the effect of B_1 inhomogeneity on CEST-SAGE-EPI sequence and incorporation of B_1 correction in future work may be beneficial.

A final potential limitation of this study was the relative inhomogeneity of the patient population, which contained untreated and recurrent glioma patients on a variety of therapies. A larger study that separates out specific treatments along with tumor grade is necessary to better understand their influence on our measurements.

6 | CONCLUSIONS

The current study presents a new CEST-SAGE-EPI sequence for obtaining high-speed, full-brain pH-sensitive and oxygen-sensitive image contrasts for brain tumor evaluation. Advantages of this technique include fast acquisition, in-line B_0 correction using phase information, whole-brain coverage, and simultaneous accurate estimation of CEST effects, R_2 , R_2^* , and R_2' . Results in tumors showed a high degree of spatial heterogeneity, and measurements were consistent with known cancer biology.

ACKNOWLEDGMENTS

American Cancer Society Research Scholar Grant (RSG-15-003-01-CCE) (B.M.E.); Art of the Brain (T.F.C.); University of California Research Coordinating Committee (B.M.E.); UCLA Jonsson Comprehensive Cancer Center Seed Grant (B.M.E.); UCLA SPORE in Brain Cancer (NIH/NCI 1P50CA211015-01A1) (B.M.E., L.M.L., P.L.N., A.L., W.B.P., T.F.C.); NIH/NCI 1R21CA223757-01 (B.M.E.)

CONFLICTS OF INTEREST

Benjamin Ellingson is on the Advisory Boards for Hoffman La-Roche, Siemens, Nativis, Medicenna, MedQIA, Bristol Meyers Squibb, Imaging Endpoints, and Agios; he is a paid consultant for Nativis, MedQIA, Siemens, Hoffman La-Roche, Imaging Endpoints, Medicenna, and Agios; and he received grant funding from Hoffman La-Roche, Siemens, Agios, and Janssen. Timothy Cloughesy is on the Advisory

Boards for Roche/Genentech, Amgen; Tocagen, NewGen, LPath, Proximagen, Celgene, Vascular Biogenics Ltd, Insys, Agios, Cortice Bioscience, Pfizer, Human Longevity, BMS, Merck, Notable Lab, and MedQIA.

ORCID

Benjamin M. Ellingson  <http://orcid.org/0000-0002-2764-6640>

REFERENCES

- [1] Gatenby RA, Gillies RJ. Why do cancers have high aerobic glycolysis? *Nat Rev Cancer*. 2004;4:891-899.
- [2] Warburg O. *The metabolism of tumours: investigations from the Kaiser Wilhelm Institute for Biology*. London: Arnold Constable; 1930.
- [3] Morita T, Nagaki T, Fukuda I, Okumura K. Clastogenicity of low pH to various cultured mammalian cells. *Mutat Res*. 1992; 268:297-305.
- [4] Gatenby RA, Vincent TL. An evolutionary model of carcinogenesis. *Cancer Res*. 2003;63:6212-6220.
- [5] Martinez-Zaguilan R, Seftor EA, Seftor RE, Chu YW, Gillies RJ, Hendrix MJ. Acidic pH enhances the invasive behavior of human melanoma cells. *Clin Exp Metastasis*. 1996;14:176-186.
- [6] Turner GA. Increased release of tumour cells by collagenase at acid pH: a possible mechanism for metastasis. *Experientia*. 1979;35:1657-1658.
- [7] Brat DJ, Castellano-Sanchez AA, Hunter SB, et al. Pseudopalisades in glioblastoma are hypoxic, express extracellular matrix proteases, and are formed by an actively migrating cell population. *Cancer Res*. 2004;64:920-927.
- [8] Lardner A. The effects of extracellular pH on immune function. *J Leukoc Biol*. 2001;69:522-530.
- [9] Shi Q, Le X, Wang B, Abbruzzese JL, Xiong Q, He Y, Xie K. Regulation of vascular endothelial growth factor expression by acidosis in human cancer cells. *Oncogene*. 2001;20:3751-3756.
- [10] Griffiths L, Dachs GU, Bicknell R, Harris AL, Stratford IJ. The influence of oxygen tension and pH on the expression of platelet-derived endothelial cell growth factor/thymidine phosphorylase in human breast tumor cells grown in vitro and in vivo. *Cancer Res*. 1997;57:570-572.
- [11] Souba WW. Glutamine and cancer. *Ann Surg*. 1993;218:715-728.
- [12] Kovacevic Z, Morris HP. The role of glutamine in the oxidative metabolism of malignant cells. *Cancer Res*. 1972;32:326-333.
- [13] Medina MA, Sanchez-Jimenez F, Marquez J, Rodriguez Quesada A, Nunez de Castro I. Relevance of glutamine metabolism to tumor cell growth. *Mol Cell Biochem*. 1992;113:1-15.
- [14] Sun PZ, Benner T, Copen WA, Sorensen AG. Early experience of translating pH-weighted MRI to image human subjects at 3 Tesla. *Stroke*. 2010;41:S147-S151.
- [15] Harris RJ, Cloughesy TF, Liau LM, et al. pH-weighted molecular imaging of gliomas using amine chemical exchange saturation transfer MRI. *Neuro Oncol*. 2015;17:1514-1524.
- [16] Harris RJ, Cloughesy TF, Liau LM, et al. Simulation, phantom validation, and clinical evaluation of fast pH-weighted molecular imaging using amine chemical exchange saturation transfer echo planar imaging (CEST-EPI) in glioma at 3 T. *NMR Biomed*. 2016;29:1563-1576.
- [17] Ogawa S, Lee TM, Kay AR, Tank DW. Brain magnetic resonance imaging with contrast dependent on blood oxygenation. *Proc Natl Acad Sci U S A*. 1990;87:9868-9872.
- [18] Fujita N, Shinohara M, Tanaka H, Yutani K, Nakamura H, Murase K. Quantitative mapping of cerebral deoxyhemoglobin content using MR imaging. *NeuroImage*. 2003;20:2071-2083.
- [19] Geisler BS, Brandhoff F, Fiehler J, et al. Blood oxygen level-dependent MRI allows metabolic description of tissue at risk in acute stroke patients. *Stroke*. 2006;37:1778-1784.
- [20] Zhang J, Chen YM, Zhang YT. Blood-oxygenation-level-dependent-(BOLD-) based R2' MRI study in monkey model of reversible middle cerebral artery occlusion. *J Biomed Biotechnol*. 2011;2011:318346.
- [21] Jensen-Kondering U, Manavaki R, Ejaz S, et al. Brain hypoxia mapping in acute stroke: back-to-back T2' MR versus (18)F-fluoromisonidazole PET in rodents. *Int J Stroke*. 2017;12: 752-760.
- [22] He X, Zhu M, Yablonskiy DA. Validation of oxygen extraction fraction measurement by qBOLD technique. *Magn Reson Med*. 2008;60:882-888.
- [23] Domsch S, Mie MB, Wenz F, Schad LR. Non-invasive multi-parametric qBOLD approach for robust mapping of the oxygen extraction fraction. *Z Med Phys*. 2014;24:231-242.
- [24] Toth V, Forschler A, Hirsch NM, et al. MR-based hypoxia measures in human glioma. *J Neurooncol*. 2013;115:197-207.
- [25] Jensen-Kondering U, Baron JC. Oxygen imaging by MRI: Can blood oxygen level-dependent imaging depict the ischemic penumbra? *Stroke*. 2012;43:2264-2269.
- [26] Hirsch NM, Toth V, Forschler A, Kooijman H, Zimmer C, Preibisch C. Technical considerations on the validity of blood oxygenation level-dependent-based MR assessment of vascular deoxygenation. *NMR Biomed*. 2014;27:853-862.
- [27] Woessner DE, Zhang S, Merritt ME, Sherry AD. Numerical solution of the Bloch equations provides insights into the optimum design of PARACEST agents for MRI. *Magn Reson Med*. 2005;53:790-799.
- [28] Liepinsh E, Otting G. Proton exchange rates from amino acid side chains—implications for image contrast. *Magn Reson Med*. 1996;35:30-42.
- [29] Bryant RG. The dynamics of water-protein interactions. *Annu Rev Biophys Biomol Struct*. 1996;25:29-53.
- [30] Schmiedeskamp H, Straka M, Newbould RD, et al. Combined spin- and gradient-echo perfusion-weighted imaging. *Magn Reson Med*. 2012;68:30-40.
- [31] Schmiedeskamp H, Straka M, Bammer R. Compensation of slice profile mismatch in combined spin- and gradient-echo echo-planar imaging pulse sequences. *Magn Reson Med*. 2012;67:378-388.
- [32] Ellingson BM, Bendszus M, Boxerman J, et al. Consensus recommendations for a standardized brain tumor imaging protocol in clinical trials. *Neuro Oncol*. 2015;17:1188-1198.

- [33] Kim M, Gillen J, Landman BA, Zhou J, van Zijl PC. Water saturation shift referencing (WASSR) for chemical exchange saturation transfer (CEST) experiments. *Magn Reson Med.* 2009;61:1441-1450.
- [34] Ellingson BM, Harris RJ, Woodworth DC, et al. Baseline pretreatment contrast enhancing tumor volume including central necrosis is a prognostic factor in recurrent glioblastoma: evidence from single and multicenter trials. *Neuro Oncol.* 2017;19:89-98.
- [35] Ellingson BM, Kim HJ, Woodworth DC, et al. Recurrent glioblastoma treated with bevacizumab: contrast-enhanced T1-weighted subtraction maps improve tumor delineation and aid prediction of survival in a multicenter clinical trial. *Radiology.* 2014;271:200-210.
- [36] Sun PZ, Wang Y, Lu J. Sensitivity-enhanced chemical exchange saturation transfer (CEST) MRI with least squares optimization of Carr Purcell Meiboom Gill multi-echo echo planar imaging. *Contrast Media Mol Imaging.* 2014;9:177-181.
- [37] Togao O, Hiwatashi A, Keupp J, et al. Scan-rescan reproducibility of parallel transmission based amide proton transfer imaging of brain tumors. *J Magn Reson Imaging.* 2015;42:1346-1353.
- [38] Heo HY, Zhang Y, Lee DH, Jiang S, Zhao X, Zhou J. Accelerating chemical exchange saturation transfer (CEST) MRI by combining compressed sensing and sensitivity encoding techniques. *Magn Reson Med.* 2017;77:779-786.
- [39] Togao O, Yoshiura T, Keupp J, et al. Amide proton transfer imaging of adult diffuse gliomas: correlation with histopathological grades. *Neuro Oncol.* 2014;16:441-448.
- [40] Song X, Xu J, Xia S, et al. Multi-echo length and offset VARied saturation (MeLOVARS) method for improved CEST imaging. *Magn Reson Med.* 2015;73:488-496.
- [41] Rohrer M, Bauer H, Mintorovitch J, Requardt M, Weinmann HJ. Comparison of magnetic properties of MRI contrast media solutions at different magnetic field strengths. *Invest Radiol.* 2005;40:715-724.
- [42] Noordin S, Winalski CS, Shortkroff S, Mulkern RV. Factors affecting paramagnetic contrast enhancement in synovial fluid: effects of electrolytes, protein concentrations, and temperature on water proton relaxivities from Mn ions and Gd chelated contrast agents. *Osteoarthritis Cartilage* 2010;18:964-970.
- [43] Mellon EA, Beesam RS, Baumgardner JE, Borthakur A, Witschey WR, Reddy R. Estimation of the regional cerebral metabolic rate of oxygen consumption with proton detected O-17 MRI during precision O-17(2) inhalation in swine. *J Neurosci Methods.* 2009;179:29-39.
- [44] Zhu XH, Zhang NY, Zhang Y, Zhang XL, Ugurbil K, Chen W. In vivo (17)O NMR approaches for brain study at high field. *NMR Biomed.* 2005;18:83-103.
- [45] Jones CK, Huang A, Xu J, et al. Nuclear Overhauser enhancement (NOE) imaging in the human brain at 7T. *NeuroImage.* 2013;77:114-124.
- [46] Perry TL, Hansen S, Berry K, Mok C, Lesk D. Free amino acids and related compounds in biopsies of human brain. *J Neurochem.* 1971;18:521-528.
- [47] Ellingson BM, Wen PY, Cloughesy TF. Evidence and context of use for contrast enhancement as a surrogate of disease burden and treatment response in malignant glioma. *Neuro Oncol.* 2017. <https://doi.org/10.1093/neuonc/nox193>.
- [48] da Ponte KF, Berro DH, Collet S, et al. In vivo relationship between hypoxia and angiogenesis in human glioblastoma: a multimodal imaging study. *J Nucl Med.* 2017;58:1574-1579.
- [49] Flynn JR, Wang L, Gillespie DL, et al. Hypoxia-regulated protein expression, patient characteristics, and preoperative imaging as predictors of survival in adults with glioblastoma multiforme. *Cancer.* 2008;113:1032-1042.
- [50] Pugh CW, Ratcliffe PJ. Regulation of angiogenesis by hypoxia: role of the HIF system. *Nat Med.* 2003;9:677-684.
- [51] Patel AP, Tirosh I, Trombetta JJ, et al. Single-cell RNA-seq highlights intratumoral heterogeneity in primary glioblastoma. *Science.* 2014;344:1396-1401.
- [52] Sottoriva A, Spiteri I, Piccirillo SG, et al. Intratumor heterogeneity in human glioblastoma reflects cancer evolutionary dynamics. *Proc Natl Acad Sci U S A.* 2013;110:4009-4014.
- [53] Maurer GD, Brucker DP, Bahr O, et al. Differential utilization of ketone bodies by neurons and glioma cell lines: a rationale for ketogenic diet as experimental glioma therapy. *BMC Cancer.* 2011;11:315.
- [54] Nie S, Li K, Huang Y, Hu Q, Gao X, Jie S. miR-495 mediates metabolic shift in glioma cells via targeting Glut1. *J Craniofac Surg.* 2015;26:e155-e158.
- [55] Wolf A, Agnihotri S, Micallef J, et al. Hexokinase 2 is a key mediator of aerobic glycolysis and promotes tumor growth in human glioblastoma multiforme. *J Exp Med.* 2011;208:313-326.
- [56] Nasrallah FA, Pages G, Kuchel PW, Golay X, Chuang KH. Imaging brain deoxyglucose uptake and metabolism by glucoCEST MRI. *J Cereb Blood Flow Metab.* 2013;33:1270-1278.
- [57] Jin T, Mehrens H, Hendrich KS, Kim SG. Mapping brain glucose uptake with chemical exchange-sensitive spin-lock magnetic resonance imaging. *J Cereb Blood Flow Metab.* 2014;34:1402-1410.
- [58] Xu X, Yadav NN, Knutsson L, et al. Dynamic glucose-enhanced (DGE) MRI: translation to human scanning and first results in glioma patients. *Tomography.* 2015;1:105-114.
- [59] Paech D, Schuenke P, Koehler C, et al. T1rho-weighted dynamic glucose-enhanced MR imaging in the human brain. *Radiology.* 2017;285:914-922.
- [60] Schuenke P, Koehler C, Korzowski A, et al. Adiabatically prepared spin-lock approach for T1rho-based dynamic glucose enhanced MRI at ultrahigh fields. *Magn Reson Med.* 2017;78:215-225.
- [61] Borodovsky A, Seltzer MJ, Riggins GJ. Altered cancer cell metabolism in gliomas with mutant IDH1 or IDH2. *Curr Opin Oncol.* 2012;24:83-89.
- [62] Stadlbauer A, Zimmermann M, Kitzwogger M, et al. MR Imaging-derived oxygen metabolism and neovascularization characterization for grading and IDH gene mutation detection of gliomas. *Radiology.* 2016:161422.
- [63] Hua J, Jones CK, Blakeley J, Smith SA, van Zijl PCM, Zhou JY. Quantitative description of the asymmetry in magnetization transfer effects around the water resonance in the human brain. *Magn Reson Med.* 2007;58:786-793.

- [64] Lee DH, Heo HY, Zhang K, et al. Quantitative assessment of the effects of water proton concentration and water T-1 changes on amide proton transfer (APT) and nuclear overhauser enhancement (NOE) MRI: the origin of the APT imaging signal in brain tumor. *Magn Reson Med*. 2017;77:855-863.
- [65] Zu ZL, Janve VA, Xu JZ, Does MD, Gore JC, Gochberg DF. A new method for detecting exchanging amide protons using chemical exchange rotation transfer. *Magn Reson Med*. 2013;69:637-647.
- [66] Zaiss M, Schmitt B, Bachert P. Quantitative separation of CEST effect from magnetization transfer and spillover effects by Lorentzian-line-fit analysis of z-spectra. *J Magn Reson*. 2011; 211:149-155.
- [67] Zaiss M, Windschuh J, Paech D, et al. Relaxation-compensated CEST-MRI of the human brain at 7T: unbiased insight into NOE and amide signal changes in human glioblastoma. *Neuro-Image*. 2015;112:180-188.
- [68] Jin T, Wang P, Zong X, Kim S-G. MR imaging of the amide-proton transfer effect and the pH-insensitive nuclear Overhauser effect at 9.4 T. *Magn Reson Med*. 2013;69:760-770.
- [69] Ulrich X, Yablonskiy DA. Separation of cellular and BOLD contributions to T2* signal relaxation. *Magn Reson Med*. 2016; 75:606-615.
- [70] Ababneh Z, Beloeil H, Berde CB, Gambarota G, Maier SE, Mulkern RV. Biexponential parameterization of diffusion and T2 relaxation decay curves in a rat muscle edema model: decay curve components and water compartments. *Magn Reson Med*. 2005;54:524-531.
- [71] Guo H, Au WY, Cheung JS. Myocardial T2 quantitation in patients with iron overload at 3 Tesla. *J Magn Reson Imaging*. 2009;30:1230-1230.

SUPPORTING INFORMATION

Additional Supporting Information may be found in the supporting information tab for this article.

FIGURE S1 Examples of B₀ correction methods available for CEST-SAGE-EPI. A, B₀ maps calculated for a single patient using phase differences from the first 2 gradient echoes acquired using CEST-SAGE-EPI. B, Corresponding B₀ maps for the same patient using the WASSR (water saturation shift referencing) method. C, Resulting maps of MTR_{asym} at 3 ppm after B₀ correction using multi-echo

phase information. D, Value of MTR_{asym} at 3 ppm after the WASSR method for B₀ correction. E, Value of MTR_{asym} at 3 ppm with no B₀ correction.

FIGURE S2 Anatomic and relaxometry MR images of human gliomas estimated using CEST-SAGE-EPI. Complementary T₂ and T₂* relaxometry images estimated from CEST-SAGE-EPI for the 4 patients illustrated in Figure 3.

FIGURE S3 Phantom results for 40 mM glutamine and 5% egg white protein. Results demonstrate increasing CEST contrast with decreasing pH, similar to those reported previously with pure glutamine phantoms. This suggests that fast-exchanging amine protons are the primary proton pool saturated using the current RF pulse scheme. Phantom preparation: Combined glutamine and protein phantoms with pH ranging from 6 to 7.5 were prepared by first adding glutamine into liquid egg white solution (5% protein) to reach concentrations of 40 mM. The pH within the sample solutions was then titrated to 6.0, 6.3, 6.6, 6.9, 7.2, and 7.4, with acid (1N HCl) and base (1N NaOH) solutions. Scan parameters: B₁ = 6 uT, TR = 5000 ms, TE1/TE2/TE3/TE4 = 14.0/34.1/58.0/92.4 ms, FOV = 217 × 240 mm, matrix size = 116 × 128, slice thickness = 4.0 mm, slice number = 10, partial Fourier encoding = 6/8, GRAPPA = 3, bandwidth = 1628 Hz/pixel with number of excitations or averages = 2. A total of 36 offset frequencies were acquired: ± 2.5 to ± 4.0 ppm with 0.1-ppm interval (± 6.0 and 20.0 ppm with respect to water proton Larmor frequency). Measurements were taken at room temperature (~20 °C). Error bars represent SD within a region of interest within the Falcon tubes.

How to cite this article: Harris RJ, Yao J, Chakhoyan A, et al. Simultaneous pH-sensitive and oxygen-sensitive MRI of human gliomas at 3 T using multi-echo amine proton chemical exchange saturation transfer spin-and-gradient echo echo-planar imaging (CEST-SAGE-EPI). *Magn Reson Med*. 2018;00:1–17. <https://doi.org/10.1002/mrm.27204>